

# Vote from the Center: 6 DoF Pose Estimation in RGB-D Images by Radial Keypoint Voting

Yangzheng Wu  
y.wu@queensu.ca

Mohsen Zand  
m.zand@queensu.ca

Ali Etemad  
ali.etemad@queensu.ca

Michael Greenspan  
michael.greenspan@queensu.ca

Department of Electrical and Computer Engineering, Ingenuity Labs,  
Queen's University, Kingston, Ontario, Canada

## Abstract

We propose a novel keypoint voting scheme based on intersecting spheres, that is more accurate than existing schemes and allows for a smaller set of more disperse keypoints. The scheme forms the basis of the proposed RCV-Pose method for 6 DoF pose estimation of 3D objects in RGB-D data, which is particularly effective at handling occlusions. A CNN is trained to estimate the distance between the 3D point corresponding to the depth mode of each RGB pixel, and a set of 3 disperse keypoints defined in the object frame. At inference, a sphere of radius equal to this estimated distance is generated, centered at each 3D point. The surface of these spheres votes to increment a 3D accumulator space, the peaks of which indicate keypoint locations. The proposed radial voting scheme is more accurate than previous vector or offset schemes, and robust to disperse keypoints. Experiments demonstrate RCVPose to be highly accurate and competitive, achieving state-of-the-art results on LINEMOD (99.7%), YCB-Video (97.2%) datasets, and notably scoring +7.9% higher than previous methods on the challenging Occlusion LINEMOD (71.1%) dataset.

## 1. Introduction

Object pose estimation is an enabling technology for many applications including robot manipulation, human-robot interaction, augmented reality, virtual reality, and autonomous driving [36, 35, 46]. It is however challenging due to background clutter, occlusions, sensor noise, varying lighting conditions, and object symmetries. Traditional methods have tackled the problem by establishing correspondences between a known 3D model and images [15, 42]. They have generally relied on hand-crafted features and therefore fail when objects are featureless or when cluttered

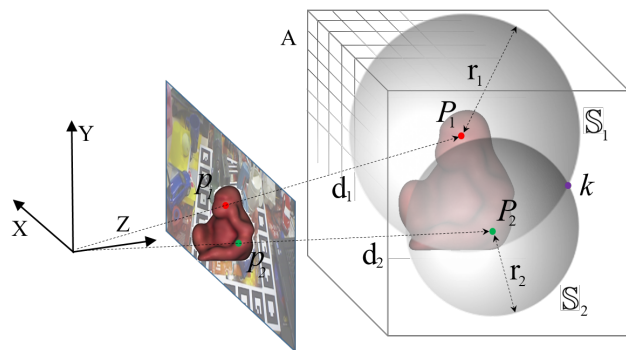


Figure 1. Radial voting scheme: 3D scene point  $P_i$  at depth  $d_i$  projects to 2D image pixel  $p_i$ . The network estimates radial distance  $r_i$  from  $p_i$ . Sphere  $S_i$  is centered at  $P_i$  with radius  $r_i$ , and all accumulator space  $A$  voxels on the surface of  $S_i$  are incremented. Keypoint  $k$  lies at the intersection of  $S_1 \cap S_2$ , and all other  $S_i$ .

tered scenes include many occluded objects [18, 36]. Recent methods typically use deep learning and train end-to-end networks to directly regress from input images to 6 DoF pose [19, 49]. Nevertheless, each object is treated as a global entity and generalization issues limit their accuracy.

More recently, CNN-based techniques have been proposed which regress 2D keypoints and use Perspective-n-Point (PnP) to estimate the 6 DoF pose parameters [35, 44]. As an alternate to directly regressing keypoint coordinates, methods which ‘vote’ for keypoints have been shown to be highly effective [36, 49, 18, 37], especially when objects are partially occluded. These schemes regress a distinct quantity that relates positions of 2D pixels to 3D keypoints, and this quantity is estimated for each pixel and cast into an accumulator space. As the votes accumulate independently for each pixel, these methods perform especially well in occluded scenes where other techniques tend to degrade.

While recent voting methods have shown great promise and leading performance, the schemes upon which they’re

based require the regression of either a 2 channel (for RGB data) [36] or 3 channel (for RGB-D data) [14] activation map. The estimation errors in each channel tend to compound, leading to reduced localization accuracy when voting for keypoints. This has motivated us to propose our novel radial voting scheme, which regresses a single channel map for RGB-D data, leading to more accurate localization. The increase in keypoint localization accuracy also allows us to disperse our keypoint set farther, which in turn increases the accuracy of object 6 DoF pose estimation.

Our proposed method trains a CNN to estimate the distance from the 3D point corresponding to each 2D RGB pixel, and a 3D object frame keypoint. At inference, this distance is estimated for each 2D scene pixel, and a sphere with this radius is centered at each corresponding 3D point. The surface of these spheres is used to increment a 3D accumulator space, and the peaks indicate keypoint location, as illustrated in Fig. 1. Executing this for minimally 3 keypoints allows the unique recovery of the 6 DoF object pose.

Our 3 main contributions are as follows: (1) We introduce the novel *radial voting scheme*, and experimentally show this to be more accurate than previous voting schemes. We further show that it maintains its accuracy for a more disperse set of keypoints, and that it is advantageous to disperse keypoints beyond the object surface, to reduce pose estimation error. (2) Based on our radial voting scheme, we propose a novel 6 DoF pose estimation method, called *RCVPose*. Notably, RCVPose requires only 3 keypoints per object, which is fewer than existing methods that use 4 or more keypoints [36, 14, 37]. (3) We experimentally characterize the performance of RCVPose on 3 standard datasets, and show that it outperforms previous peer reviewed methods. We also conduct ablation studies to justify certain design decisions and hyper-parameter settings. Our implementation is made publicly available [1].

## 2. Related Work

Estimating 6 DoF pose has been extensively addressed in the literature [25, 15, 49, 4]. Recent deep learning-based methods that use CNNs to generate object poses can be generally classified into three categories: keypoint-based [49], viewpoint-based [15], and voting-based methods [37].

**Keypoint-based methods** detect specified keypoints and apply the Perspective-n-Point (PnP) algorithm for final pose estimation. Hu *et al.* [18] proposed a segmentation-driven 6 DoF pose estimation method which used the visible parts of objects for local pose prediction from 2D keypoint locations. They then used the output confidence scores of a YOLO-based [41] network to establish 2D to 3D correspondences between the image and the object’s 3D model. Zakharov *et al.* [50] proposed a dense pose object detector to estimate dense 2D-3D correspondence maps between an input image and available 3D models, recovering 6 DoF pose

using PnP and RANSAC. In addition to RGB data, extra depth information was used in [14] to detect 3D keypoints of objects via a deep Hough voting network, with the 6 DoF pose parameters then fit with a least-squares method.

**Viewpoint-based methods** predict 6 DoF poses without textured models. In [33], a generative auto-encoder architecture used a GAN to convert RGB images into 3D coordinates, similar to the image-to-image translation task. Generated pixel-wise predictions were used in multiple stages to form 2D-3D correspondences to estimate poses with RANSAC-based PnP. Manhardt *et al.* [26] proposed predicting several 6 DoF poses for each object instance to estimate the pose distribution generated by symmetries and repetitive textures. Each predicted hypothesis corresponded to a single 3D translation and rotation, and estimated hypotheses collapsed onto the same valid pose when the object appearance was unique. Other recent variations of this method include Trabelsi *et al.* [45], who used a multi-task CNN-based encoder/multi-decoder network, and Wang *et al.* [48] and [20, 34, 43], who used a rendering method by a self-supervised model on unannotated real RGB-D data to find a visually and geometrically optimal alignment.

**Voting-based methods** have a long history in pose estimation. Before the use of artificial intelligence became widespread, first the Hough Transform [7] and RANSAC [10] and subsequently methods such as pose clustering [31] and geometric hashing [21] were widely used to localize both simple geometric shapes and full 6 DoF object pose. Hough Forests [11], while learning-based, still required hand-crafted feature descriptors. Voting was also extended to 3D point cloud images, such as 4PCS [2] and its variations [29, 28], which used RANSAC-style congruent extraction to estimate affine-invariant poses.

Following the advent of CNNs, hybrid methods emerged which combined aspects of both CNN and classical approaches. Both [18] and [36] conclude with RANSAC-based keypoint voting, whereas Deep Hough Voting [37] proposed a complete MLP pipeline of keypoint localization using a series of convolutional layers as the voting module. To estimate keypoint positions, two different deep learning-based voting schemes have appeared [36, 49, 18, 37], the proposed scheme introducing a third. At training, all three schemes regress a distinct quantity that relates positions of pixels to keypoints. At inference, this quantity is estimated for each pixel, and is cast into an accumulator space in a voting process. Accumulator spaces can be 2D [49, 18, 37] representing image space, or more recently 3D [36] representing the camera reference frame. Following voting, peaks in accumulator space indicate the positions of the keypoints in the 2D image or 3D camera frame.

While only a few hybrid voting-based methods exist for 6 DoF pose estimation, they have outstanding performance, which has motivated us to develop RCVPose as a further

advance of this class of hybrid method. Specifically, our method is inspired by PVNet [36], and is most closely related to the recently proposed PVN3D of He *et al.* [14], which combined PVNet and Deep Hough Voting [37] with a 3D accumulator space, applying the offset voting scheme of [49].

### 3. Methodology

#### 3.1. Keypoint Voting Schemes

Let  $p_i$  be pixel from RGB-D image  $I$  with 2D image coordinate  $(u_i, v_i)$  and corresponding 3D camera frame coordinate  $(x_i, y_i, z_i)$ . Further let  $k_j^\theta = (x_j, y_j, z_j)$  denote the camera frame coordinate of the  $j^{\text{th}}$  keypoint of an object located at 6 DoF pose  $\theta$ . The quantity  $\mathbf{m}_o$  regressed in the first *offset* scheme [18, 37] is the displacement between the two points, which in the 3D case is denoted as:

$$\mathbf{m}_o = (\Delta x, \Delta y, \Delta z) = (x_i - x_j, y_i - y_j, z_i - z_j) \quad (1)$$

Alternately, the 3D quantity  $\mathbf{m}_v$  from the second *vector* scheme [36, 49] is the unit vector pointing to  $k_j^\theta$  from  $p_i$ :

$$\mathbf{m}_v = (dx, dy, dz) = \frac{\mathbf{m}_o}{\|\mathbf{m}_o\|} \quad (2)$$

Finally, the quantity  $\mathbf{m}_r$  from the third *radial* scheme proposed here is the 1D Euclidean distance between the points:

$$\mathbf{m}_r = \|\mathbf{m}_o\| \quad (3)$$

#### 3.2. Keypoint Estimation Pipeline

The above described three voting schemes can be used interchangeably within a keypoint estimation pipeline. The inputs to the training process (shown in Fig. 2) are: the RGB fields  $I^{RGB}$  of image  $I$ ; ground truth binary segmented image  $S$  of the foreground object at pose  $\theta$ ; ground truth keypoint coordinate  $k_j^\theta$ ; and the calculated ground truth values  $\mathbf{m}_{\{o|v|r\}}$  for each pixel in  $S$ , represented by matrix  $M_1$ .  $M_1$  is calculated for a given  $\theta$  and  $k_j^\theta$  using Eqs. 1, 2 or 3, and has channel depth 3 for each of the 3D offset ( $\mathbf{m}_o$ ) and vector ( $\mathbf{m}_v$ ) schemes, and depth 1 for the 1D radial ( $\mathbf{m}_r$ ) scheme. Both  $S$  and  $M_1$  are accessed to compute the loss:

$$\mathcal{L} = \mathcal{L}_S + \mathcal{L}_{M_1}, \quad (4)$$

$$\mathcal{L}_S = \frac{1}{N} \sum_{i=1}^N \left| \hat{S}_i - S_i \right|, \quad (5)$$

$$\mathcal{L}_{M_1} = \frac{\sum_{i=1}^N \left( |\hat{M}_{1i} - M_{1i}| \cdot S_i \right)}{\sum_{i=1}^N S_i}, \quad (6)$$

with summations over all  $N$  pixels. The network output is estimate  $\hat{S}$  of  $S$ , and (unsegmented) estimate  $\hat{M}_0$  of  $M_1$ .

At inference, as shown in Fig. 2,  $I^{RGB}$  is input to the network which returns estimates  $\hat{S}$  and  $\hat{M}_0$ , the element-wise multiplication of which results in segmented estimate  $\hat{M}_1$ . Each  $(u_i, v_i)$  element of  $\hat{M}_1$ , with corresponding 3D coordinate  $(x_i, y_i, z_i)$  drawn from the depth field  $I^D$  of  $I$ , then independently casts a vote through the voting module into the initially empty 3D accumulator space  $A$ . Specific to each voting scheme, for every  $(u_i, v_i)$ :

- **Offset** voting: Accumulator element  $A[x_i + \hat{M}_1[u_i, v_i, 0], y_i + \hat{M}_1[u_i, v_i, 1], z_i + \hat{M}_1[u_i, v_i, 2]]$  is incremented, thereby voting for the element containing keypoint  $k_j^\theta$ ;
- **Vector** voting: Every accumulator element is incremented that intersects with the ray  $\alpha(x_i + \hat{M}_1[u_i, v_i, 0], y_i + \hat{M}_1[u_i, v_i, 1], z_i + \hat{M}_1[u_i, v_i, 2])$ , for  $\alpha > 0$ , thereby voting for every element on the ray that intersects with  $(x_i, y_i, z_i)$  and  $k_j^\theta$ ;
- **Radial** voting: Every accumulator element is incremented that intersects with the sphere of radius  $\hat{M}_1[u_i, v_i]$  centered at  $(x_i, y_i, z_i)$ , thereby voting for every element that lies on the surface of a sphere upon which  $k_j^\theta$  resides.

The basis of radial voting is shown in Fig. 1. Whichever voting scheme is used, at the conclusion of the voting module, a global peak will exist at that element of  $A$  that contains  $k_j^\theta$ , and so a simple peak detection operation is then sufficient to estimate keypoint position  $\hat{k}_j^\theta$ .

#### 3.3. Preliminary Considerations

We conduct an experiment to evaluate the relative accuracies of the three voting schemes at keypoint localization, using the process from Sec. 3.2. Each scheme used the same 15%/85% train/test split of a subset of objects from the LINEMOD dataset. All three schemes used the exact same backbone network and hyper-parameters. Specifically, they all used a fully convolutional ResNet-18 [24], batch size 48, initial learning rate 1e-3, and Adam optimizer, with accumulator space resolution of 1 mm. They were all trained with a fixed learning rate reduction schedule, which reduced the rate by a factor of 10 following every 70 epochs, and all trials trained until they fully converged.

The only difference between trials, other than the selective use of Eqs. 1-3 in the calculation of  $\hat{M}_1$  at training to select a particular voting scheme, was a slight variation in the loss functions. For offset and radial voting, the L1 loss from Eqs. 4-6 was used, identical to the offset voting in PVN3D [14]. Alternately, the Smooth L1 equivalents of Eqs. 5 and 6 (with  $\beta=1$ ) were used for vector voting, as in PVNet [36] (albeit therein using a 2D accumulator space).

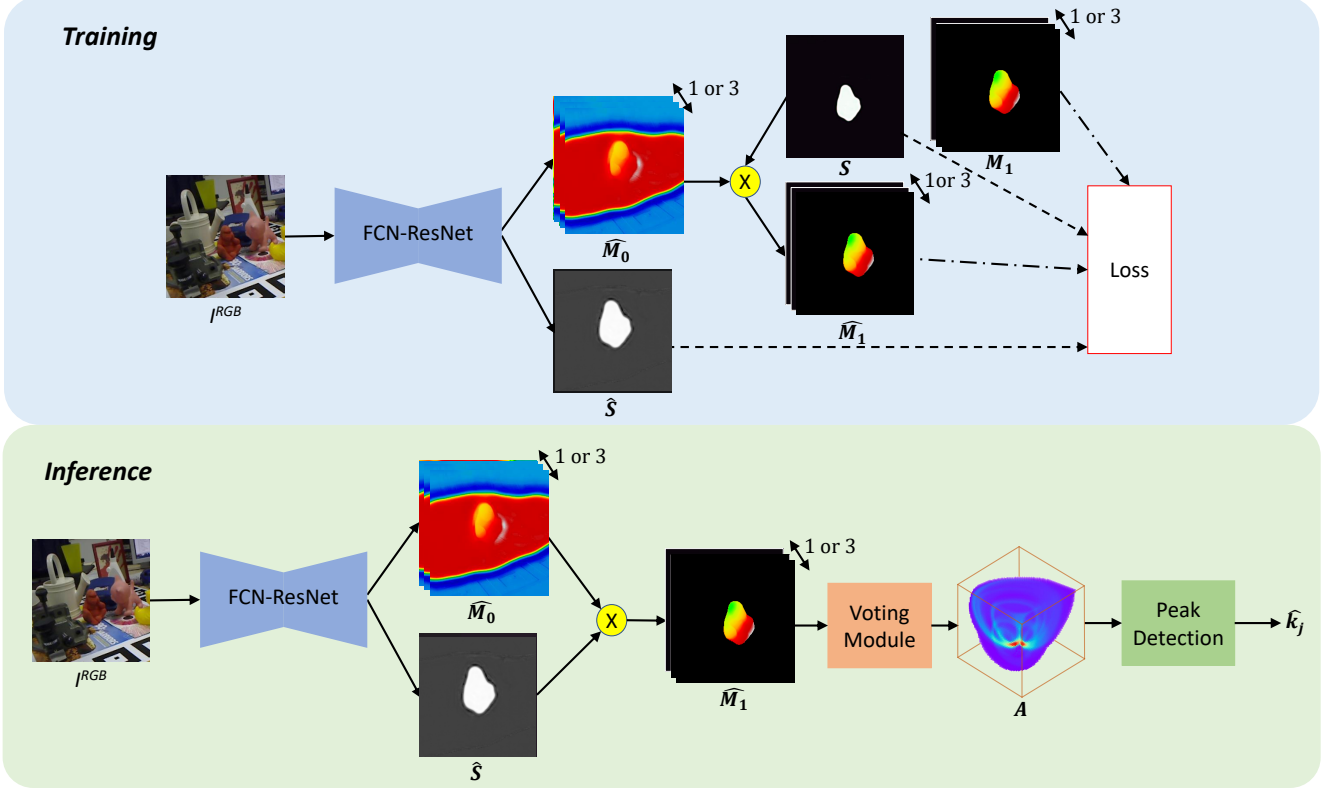


Figure 2. RCVPose training and inference

Sets of size  $K=4$  surface keypoints were selected for each object tested, using the Farthest Point Sampling method [9] (*FPS*). *FPS* selects  $K$  points on the surface of an object which are well separated, and is a popular keypoint generation strategy [36, 14, 38, 37]. Following training, each keypoint’s location  $\hat{k}_j^{\theta_i}$  was estimated by propagating each test image  $I_i$  through the network, as in Fig. 2. The error  $\epsilon_{i,j}$  for each estimate was determined by its Euclidean distance from its ground truth location, i.e.  $\epsilon_{i,j} = \|\hat{k}_j^{\theta_i} - k_j^{\theta_i}\|$ . The average of  $\epsilon_{i,j}$  for an object over all test images and keypoints was the *keypoint estimation error*, denoted as  $\bar{\epsilon}$ .

Each of the three voting schemes was implemented with care, so that they were numerically accurate and equivalent. To test the correctness of voting in isolation, ground truth values of  $M_1$  calculated for each object and scheme were passed directly into the voting module, effectively replacing  $\hat{M}_1$  with  $M_1$  in the inference stage of Fig. 2. For each voting scheme, the average  $\bar{\epsilon}$  for all objects was similar and less than the accumulator space resolution of 1 mm, indicating that the implementations were correct and accurate.

The  $\bar{\epsilon}$  values were evaluated for the three voting schemes for the ape, drill and eggbox objects as summarized in Table 1. These three particular objects were chosen as the ape is the smallest, and the drill the largest of the LINEMOD

objects, and eggbox includes a rotational symmetry. Table 1 includes a measure of the average distance  $\bar{r}$  of the ground truth keypoints to each object centroid. Radial voting is seen to be the most accurate method, with a mean value between 3x and 4.5x more accurate than offset voting, and between 4.4x and 7.7x more accurate than vector voting. Radial voting also has a smaller standard deviation than either other method. Offset voting is more accurate than vector voting, the ordinal relationship between the three schemes remaining consistent across the objects.

This experiment was repeated for keypoints selected from the corners of an object’s bounding box, which was first scaled by a factor of 2 so that the keypoints were dispersed to fall outside of the object’s surface. The results in Table 2 indicate that radial voting still outperforms the other two schemes by a large margin. Further, whereas the other two methods decrease in accuracy significantly as the mean keypoint distance  $\bar{r}$  increases, radial voting accuracy degrades more gracefully. For example, for the ape, the 232% increase in  $\bar{r}$  from 61.2 to 142.1 mm, reduced accuracy for offset voting by 80% (from 5.8 to 10.4 mm), but only by 23% (from 2.2 to 2.7 mm) for radial voting.

The improved accuracy of radial voting is likely due to the fact that the radial scheme regresses a 1D quantity, whereas the offset and vector schemes regress 3D quantities, with the errors in each independent dimension com-



	$\bar{r}$ [mm]	$\bar{\epsilon}$ [mm]					
		vector		offset		radial	
		$\mu_v$	$\sigma_v$	$\mu_o$	$\sigma_o$	$\mu_r$	$\sigma_r$
ape	61.2	10.0	5.8	5.8	2.6	<b>1.3</b>	<b>0.7</b>
driller	129.4	10.0	2.3	6.5	4.7	<b>2.2</b>	<b>1.0</b>
eggbox	82.5	11.8	5.3	5.2	2.7	<b>2.0</b>	<b>0.7</b>

Table 1. Surface keypoint estimation error:  $\bar{\epsilon}$  mean ( $\mu_{\{v|o|r\}}$ ) and standard deviation ( $\sigma_{\{v|o|r\}}$ ) for 3 voting schemes, with  $\bar{r}$  = mean distance of keypoints to object centroid.

	$\bar{r}$ [mm]	$\bar{\epsilon}$ [mm]					
		vector		offset		radial	
		$\mu_v$	$\sigma_v$	$\mu_o$	$\sigma_o$	$\mu_r$	$\sigma_r$
ape	142.1	12.5	7.6	10.4	5.3	<b>1.8</b>	<b>0.8</b>
driller	318.8	11.3	8.2	9.5	3.5	<b>2.7</b>	<b>0.8</b>
eggbox	197.3	13.7	8.5	11.4	4.7	<b>2.4</b>	<b>1.2</b>

Table 2. Dispersed keypoint estimation error:  $\bar{\epsilon}$  mean ( $\mu_{\{v|o|r\}}$ ) and standard deviation ( $\sigma_{\{v|o|r\}}$ ) for 3 voting schemes, with  $\bar{r}$  = mean distance of keypoints to object centroid.

pounding during voting. Radial voting also has a degree of resilience to in-plane rotations which is lacking in offset or vector voting. The larger inaccuracies of vector voting likely draw from the fact that small angular errors result in larger positional errors when projected over a distance.

### 3.4. Keypoint Dispersion to Improve Pose Accuracy

It was suggested in [14] that the accuracy of 6 DoF pose parameter estimation can be improved by selecting keypoints that lie on the object surface, rather than the corners of bounding boxes which lie beyond the object surface. While this is certainly the case if the localization errors increase significantly with keypoint distance (as with vector and offset voting), there is actually an advantage to dispersing the keypoints farther apart, were such localization error to be eliminated or reduced (as with radial voting).

To demonstrate this, we executed an experiment in which the keypoint locations were dispersed to varying degrees under a constant keypoint estimation error, with the impact measured on the accuracy of the estimated pose. We first selected a set  $\mathcal{K} = \{k_j\}_{j=1}^4$  keypoints from the surface of an object, using the FPS strategy. This set was then rigidly transformed by  $T$ , comprising a random rotation (within  $0^\circ$  to  $360^\circ$  for each axis) and a random translation (within  $1/2$  of the object radius), to form keypoint set  $\mathcal{K}_T$ . Each keypoint in  $\mathcal{K}_T$  was then independently perturbed by a magnitude of 1.5 mm in a random direction, to simulate the keypoint localization error of the radial voting scheme, resulting in keypoint set  $\tilde{\mathcal{K}}_T$ .

Next, the transformation  $\tilde{T}$  between  $\tilde{\mathcal{K}}_T$  and the original (untransformed and unperturbed) keypoint set  $\mathcal{K}$  was calculated using the Horn method [17]. This process simulates the pose estimation that would occur between estimated keypoint locations, each of which contains some error, and their corresponding ground truth model keypoints. The sur-

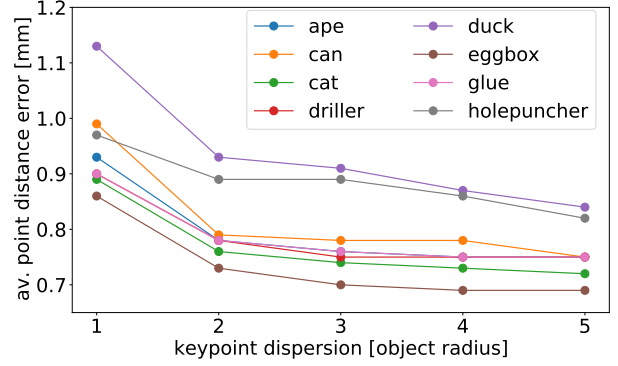


Figure 3. Average point distance error ( $\bar{\epsilon}$  [mm]) vs. keypoint dispersion [object radius].

face points of the object were then transformed by both the ground truth  $T$  and the estimated  $\tilde{T}$  transformations, and the distances separating corresponding transformed surface points were compared.

The above process was repeated for versions of  $\mathcal{K}$  that were dispersed through scaling them an integral factor of the object radius from the object centroid. The exact same error perturbations (i.e. magnitudes and directions) were applied to each distinct keypoint for each new scale value. The scaled trials therefore represented keypoints that were dispersed more distant from the object centroid, albeit with the exact same localization error.

This process was executed for all Occlusion LINEMOD objects, with 100 trials for each scale factor value from 1 to 5. The means of the corresponding point distances (i.e. the ADD metric as defined in [15]) are plotted in Fig. 3. It can be seen that ADD decreases for the first few scale factor increments for all objects, indicating an increase in pose estimation accuracy for larger keypoint dispersions. This increase in accuracy stems from improved rotational estimates, as the same positional perturbation error of a keypoint under a larger moment arm will result in a smaller angular error. The translational component of the transformation is not impacted by the scaling, as the Horn method starts by centering the two point clouds. After a certain increase in scale factor of 3 or 4, the unaffected translational error dominates, and the error plateaus.

This experiment indicates that, so long as keypoint localization error remains small, then 6 DoF pose estimation error is reduced by dispersing the keypoints so that they fall  $\sim 1$  object radius beyond the surface of the object.

### 3.5. RCVPose

The above described voting method formed the core of our RCVPose pose estimation process. The radial voting scheme was used, based on its superior accuracy as demonstrated in Sec. 3.3. The network of Fig. 2 was used with ResNet-152 serving as the FCN-ResNet module.

The minimal  $K=3$  keypoints were used for each object,

selected from the corners of each object’s bounding box. Based on Sec. 3.4, these keypoints were scaled to lie beyond the surface of each object, at a distance of 2 object radius units from its centroid. For each object, 3 instances of the network were trained, one for each keypoint.

Once the  $K=3$  keypoint locations are estimated for an image, it is straightforward to determine the object’s 6 DoF rigid transformation  $\theta$ , by passing the corresponding estimated scene and ground truth object keypoint coordinates to the Horn [17] or an equivalent [8] method. This is analogous to the approach of [14], and differs from previous pure RGB approaches [36] which require the iterative optimization of a PnP method through RANSAC. In contrast, the transformation recovery here and in [14] are non-iterative and therefore efficient.

### 3.6. Implementation Details

**Preprocessing, Network Structure and Training:** Prior to training, each RGB image is shifted and scaled to adhere to the ImageNet mean and standard deviation [6]. The 3D coordinates are then calculated from the image depth fields and represented in decimeter units, as all LINEMOD and YCB-Video objects are at most 1.5 decimeters in diameter.

The network structure was based on a Fully Convolutional ResNet-152 [13], similar to PVNet [36], albeit with two main differences. First, we replaced LeakyReLU with ReLU as the activation function. This was because our radial voting scheme only includes positive values, in contrast to the vector voting scheme of PVNet which admits both positive and negative values. The second difference, illustrated in Fig. 4, is that we added more skip connections linking the downsampling and upsampling layers, to enhance the impact of additional local features when up-sampling [24].

The loss functions of Eqs. 4-6 were used with an Adam optimizer, with an initial learning rate of  $lr=1e-4$ . The  $lr$  was adjusted on a fixed schedule, re-scaled by a factor of 0.1 every 70 epochs. The network was trained for 300 and 500 epochs for each object in the LINEMOD and YCB-Video datasets respectively, with batch size 32 for all training runs.

**Accumulator Space and Radial Voting:** The accumulator space  $A$  is represented as a flat 3D integer array, i.e. an axis-aligned grid of voxel cubes. The size of  $A$  was set for each test image to the bounding box of the 3D data. The voxel resolution was set to 5 mm, which was found to be a good tradeoff between memory expense and keypoint localization accuracy (see Sec. D).

All voxels were initialized to zero, with their values incremented as votes were cast. The voting process is similar to 3D sphere rendering, wherein those voxels that intersect with the sphere surface have their values incremented. The process is based on Andre’s circle rendering algorithm [3]. We generate a series of 2D slices of  $A$  parallel to the x-y

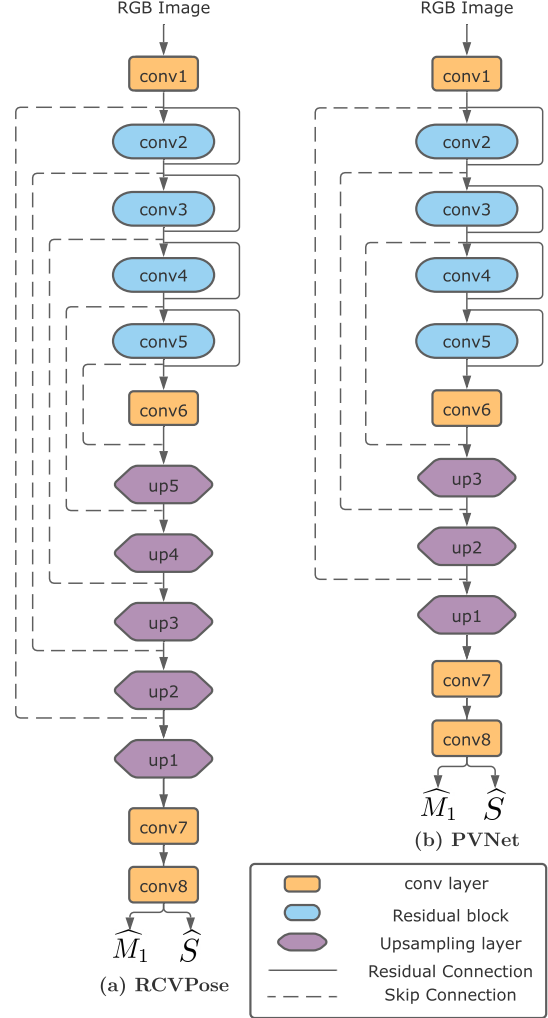


Figure 4. Backbone network structure for (a) RCVPose and (b) PVNet: Denser skip connections allow more local image features to be kept during upsampling.

plane, that fall within the sphere radius from the sphere center in both directions of the z-axis. For each slice, the radius of the circle formed by the intersection of the sphere and that slice is calculated, and all voxels that intersect with this circumference are incremented. The algorithm is accurate and efficient, requiring that only a small portion of the voxels be visited for each sphere rendering. It was implemented in Python and parallelized at the thread level, and executes with an efficiency similar to forward network inference.

## 4. Experiments

### 4.1. Datasets

The LINEMOD dataset [15] includes 1200 images per object. The training set contained only 180 training samples using the standard 15%/85% training/testing split [49, 36, 5, 14, 18]. We augmented the dataset by rendering the

objects with a random rotation and translation, transposed using the BOP rendering kit [16] onto a background image drawn from the MSCOCO dataset [23]. An additional 1300 augmented images were generated for each object in this way, inflating the training set to 1480 images per object.

The LINEMOD depth images have an offset compared to the ground-truth pose values, for unknown reasons [27]. To reduce the impact of this offset, we regenerated the depth field for each training image from the ground truth pose, by reprojecting the depth value drawn from the object pose at each 2D pixel coordinate. The majority (1300) of the resulting training set were in this way purely synthetic images, and the minority (180) comprised real RGB and synthetic depth. All test images were original, real and unaltered.

**Occlusion LINEMOD** [4] is a re-annotation of LINEMOD comprising a subset of 1215 challenging test images of objects under partial occlusion. The protocol is to train the network on LINEMOD images only, and then test on Occluded LINEMOD to verify robustness.

**YCB-Video** [49] is a much larger dataset, containing 130K key frames of 21 objects over 92 videos. We split 113K frames for training and 27K frames for testing, following PVN3D [14]. For data augmentation, YCB-Video provides 80K synthetic images with random object poses, rendered on a black background. We repeated here the process described above, by rendering random MSCOCO images as background. The complete training dataset therefore comprised 113K real + 80K synthetic = 193K images.

## 4.2. Evaluation Metrics

We follow the ADD and ADDs (i.e. ADD(s)) metrics defined by [15] to evaluate LINEMOD, whereas YCB-Video is evaluated based on ADD(s) and AUC as proposed by [49]. All metrics are based on the distances between corresponding points as objects are transformed by the ground truth and estimated transformations. ADD measures the average distance between corresponding points, whereas ADDs averages the minimum distance between closest points, and is more forgiving for symmetric objects. A pose is considered correct if its ADD(s) falls within 10% of the object radius. AUC applies the ADD(s) values to determine the success of an estimated transformation, integrating these results over a varying 0 to 100 mm threshold.

## 4.3. Results

We achieved state-of-art results on all three datasets, under a moderate training effort (i.e. hyper-parameter adjustment). The most challenging dataset was Occlusion LINEMOD, the results for which are listed in Table 3. RCVPose+ICP outperformed all other methods on average, achieving 71.1% mean accuracy, exceeding the next closest method PVN3D by 7.9%. It achieved the top performance on all objects except duck, where PVNet had the best result.

Mode	Method	ADD(s) [%]	
		LINEMOD	Occ. LINEMOD
RGB	SSD6D [19]	9.1	-
	Oberweger [30]	-	27.1
	Hu et al. [18]	-	30.4
	Pix2Pose [33]	72.4	32.0
	DPOD [50]	83.0	32.8
	PVNet [36]	86.3	40.8
	DeepIM [22]	88.6	-
	PPRN [45]	93.9	58.4
RGB +D ref	YOLO6D [44]	56.0	6.4
	SSD6D+ref [19]	34.1	27.5
	PoseCNN [49]	-	24.9
	DPOD+ref [50]	95.2	47.3
RGB-D	DenseFusion [47]	94.3	-
	PVN3D [14]	99.4	63.2
	RCVPose	99.4	70.2
	RCVPose+ICP	<b>99.7</b>	<b>71.1</b>

Table 3. LINEMOD and Occlusion LINEMOD accuracy results.

Even without ICP refinement, RCVPose achieved close to the same results at 70.2% mean accuracy.

One advantage of RCVPose is its scale tolerance. Unlike most other methods whose performance reduced with smaller objects, our method was not impacted much. Significantly, it improved the accuracy over PVN3D from 33.9%, 39.1% to 61.3%, 39.1% for the ape and cat, respectively. Another advantage is it accumulates votes independently for each pixel and is therefore robust to partial occlusions, exhibiting the ability to recognize objects that undergo up to 70% occlusion, as in Fig. 5.

The LINEMOD dataset is less challenging, as the labelled objects are unoccluded. As listed in Table 3, RCVPose+ICP still achieved the highest mean accuracy of 99.7%, slightly exceeding the tie between RCVPose (without ICP) and PVN3D. RCVPose+ICP was the only method to achieve 100% accuracy for more than one object. Again the RGB-D methods outperformed all other data modes, and the top performing RGB method that included depth refinement (i.e. *RGB+D ref*) outperformed the best pure RGB method, supporting the benefits of the depth mode.

The YCB-Video results in Table 4 list the AUC and ADD(s) metrics, both with and without depth refinement. RCVPose is the top performing method, achieving between 95.2% and 95.9% ADD(s) and between 96.6% and 97.2% AUC accuracy, outperforming the next best method PVN3D by at least 3.4% ADD(s) and 1.1% AUC. Notably, RCVPose increased the ADD(s) accuracy of the relatively small tuna fish can by a full 6%.

## 4.4. Ablation Studies

**Accumulator Space Resolution:** We experimented with different resolutions of the accumulator space, to evaluate

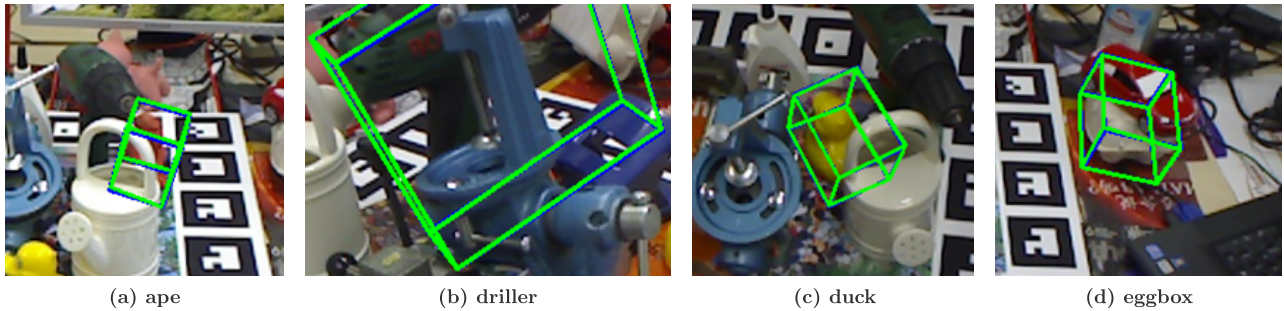


Figure 5. Ocluded LINEMOD sample results: Blue box = ground truth, green box = estimate. RCVPose is robust to occlusion even in some severe cases.

Refine?	Method	ADD(s) [%]	AUC [%]
No	PoseCNN [49]	59.9	75.8
	DF (per-pixel) [47]	82.9	91.2
	PVN3D [14]	91.8	95.5
	RCVPose	<b>95.2</b>	<b>96.6</b>
Yes	PoseCNN [49]	85.4	93.0
	DF (iterative) [47]	86.1	93.2
	PVN3D [14]+ICP	92.3	96.1
	RCVPose+ICP	<b>95.9</b>	<b>97.2</b>

Table 4. YCB-Video accuracy results.

$\rho$ [mm]	$\bar{\epsilon}$ [mm]		ADD [%]	speed [fps]	memory [Mbyte]
	$\mu_r$	$\sigma_r$			
1	1.75	0.81	61.5	5	$4 \times 479^3 = 440$
2	2.33	0.52	61.3	12	$4 \times 239^3 = 55$
4	6.27	0.72	61.3	20	$4 \times 118^3 = 6.5$
5	6.33	0.69	61.3	24	$4 \times 95^3 = 3.4$
8	11.73	2.37	55.2	32	$4 \times 58^3 = 0.8$
16	17.92	5.52	45.7	40	$4 \times 28^3 = 0.09$

Table 5. Accumulator space resolution  $\rho$  [mm] impact on accuracy  $\bar{\epsilon}$  [mm], ADD [%], processing speed [fps], and memory [Mbyte], for LINEMOD ape test images. The processing speed includes only the accumulator space time performance.

the balance of accuracy and efficiency. Resolution  $\rho$  refers to the linear dimension of a voxel edge (i.e. voxel volume  $= \rho^3$ ). We selected 6 different resolutions from  $\rho = 1$  mm to 16 mm, and ran the voting module for each  $\rho$  value with the same system, for all 3 scaled bounding box keypoints of all test images of the LINEMOD ape object (as in Table 2).

The results are listed in Table 5 which shows the means  $\mu_r$  and standard deviations  $\sigma_r$  of the keypoint estimation errors  $\bar{\epsilon}$  and ADD metric, and both the time and space efficiencies, for varying voxel resolutions. As expected, the voting module was faster and smaller, and the keypoint estimation error was greater, at coarser resolutions. The ADD value, which is the main metric used to identify a successful pose estimation event, remains nearly constant up to a resolution of 5 mm. The  $\rho = 5$  mm voxel size therefore achieved both an acceptable speed of 24 fps, an efficient memory footprint of 3.4 Mbytes, and close to the highest ADD value, and so

	Number of Keypoints		
	3	4	8
ape	61.3	60.9	61.3
driller	78.8	78.6	78.8
eggbox	82.3	82.6	82.3

Table 6. Accuracy w.r.t. Number of Keypoints

it was subsequently used throughout the experiments.

**Number of Keypoints:** Previous works have used a minimum of 4 [35], and up to 8 [14, 36] or more [37] keypoints per object, selected from the corners of the object bounding box [40, 44, 32] or using the FPS algorithm [37, 14, 36]. It has been suggested that a greater number of keypoints is preferable to improve robustness and accuracy [14, 36], especially for pure RGB methods in which at least 3 keypoints need to be visible for any view of an object to satisfy the constraints of the P3P algorithm [39, 12].

We experimented with the impact of the number of keypoints on pose estimation accuracy. Sets of 3, 4 and 8 keypoints were selected for the ape, driller and eggbox LINEMOD objects, using the Bounding Box selection method described in Sec. 3.4. The results shown in Fig. 6 and Table. 6 indicate that increasing the number of RCV-Pose keypoints does not impact pose estimation accuracy, which changed at most only 0.4% between these settings for all three objects. This is likely due to the accuracy with which the radial voting scheme is able to estimate keypoint locations, which removes the added benefit of redundant keypoints. Given that the time and memory expense scale linearly with the number of keypoints, we settled upon the use of the minimal 3 keypoints for RCVPose for all of our experiments.

#### 4.5. Time Performance

RCVPose runs at 18 fps on a server with an Intel Xeon 2.3 GHz CPU and RTX8000 GPU for a  $640 \times 480$  image input. This compares well to other voting-based methods,



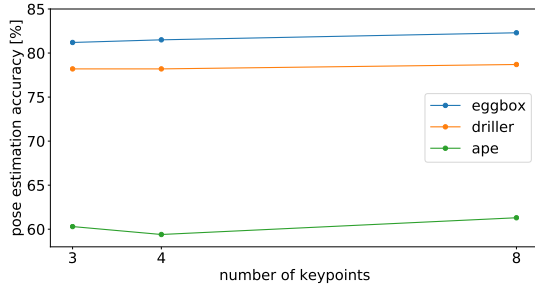


Figure 6. Pose estimation accuracy [mm] vs. number of keypoints.

such as PVNet at 25 fps, and PVN3D at 5 fps. The backbone network forward path, the radial voting process and the Horn transformation solver take 10, 41, and 4 msec. per image respectively at inference time.

## 5. Conclusion

We have proposed RCVPose, a hybrid 6 DoF pose estimator with a fully convolutional ResNet-based radial estimator and a novel keypoint radial voting scheme. Our radial voting scheme is shown to be more accurate than previous schemes, especially when the keypoints are more dispersed, which leads to more accurate pose estimation requiring only 3 keypoints. We achieved state-of-the-art results on three popular benchmark datasets, YCB-Video, LINEMOD and the challenging Occlusion LINEMOD, with an 18 fps run-time.

## References

- [1] withheld to preserve author anonymity during paper review. 2
- [2] D. Aiger, N. J. Mitra, and D. Cohen-Or. 4-points congruent sets for robust surface registration. *ACM Transactions on Graphics*, 27(3):#85, 1–10, 2008. 2
- [3] Eric Andres. Discrete circles, rings and spheres. *Computers & Graphics*, 18(5):695–706, 1994. 6
- [4] Eric Brachmann, Alexander Krull, Frank Michel, Stefan Gumhold, Jamie Shotton, and Carsten Rother. Learning 6d object pose estimation using 3d object coordinates. In *European conference on computer vision*, pages 536–551. Springer, 2014. 2, 7
- [5] Yannick Bukschat and Marcus Vetter. Efficientpose—an efficient, accurate and scalable end-to-end 6d multi object pose estimation approach. *arXiv preprint arXiv:2011.04307*, 2020. 6
- [6] J. Deng, W. Dong, R. Socher, L. Li, Kai Li, and Li Fei-Fei. Imagenet: A large-scale hierarchical image database. In *2009 IEEE Conference on Computer Vision and Pattern Recognition*, pages 248–255, 2009. 6
- [7] Richard O Duda and Peter E Hart. Use of the hough transformation to detect lines and curves in pictures. *Communications of the ACM*, 15(1):11–15, 1972. 2
- [8] A. Eggert and Robert Fisher. A comparison of four algorithms for estimating 3-d rigid transformations. 05 1998. 6
- [9] Yuval Eldar, Michael Lindenbaum, Moshe Porat, and Yehoshua Y Zeevi. The farthest point strategy for progressive image sampling. *IEEE Transactions on Image Processing*, 6(9):1305–1315, 1997. 4
- [10] Martin A Fischler and Robert C Bolles. Random sample consensus: a paradigm for model fitting with applications to image analysis and automated cartography. *Communications of the ACM*, 24(6):381–395, 1981. 2
- [11] J. Gall, A. Yao, N. Razavi, L. Van Gool, and V. Lempit-sky. Hough forests for object detection, tracking, and action recognition. *IEEE Transactions on Pattern Analysis and Machine Intelligence*, 33(11):2188–2202, 2011. 2
- [12] X. Gao, Xiaorong Hou, Jianliang Tang, and H. Cheng. Complete solution classification for the perspective-three-point problem. *IEEE Trans. Pattern Anal. Mach. Intell.*, 25:930–943, 2003. 8
- [13] Kaiming He, Xiangyu Zhang, Shaoqing Ren, and Jian Sun. Deep residual learning for image recognition. In *Proceedings of the IEEE conference on computer vision and pattern recognition*, pages 770–778, 2016. 6, 12
- [14] Yisheng He, Wei Sun, Haibin Huang, Jianran Liu, Haoqiang Fan, and Jian Sun. Pvn3d: A deep point-wise 3d keypoints voting network for 6dof pose estimation. In *Proceedings of the IEEE/CVF Conference on Computer Vision and Pattern Recognition (CVPR)*, June 2020. 2, 3, 4, 5, 6, 7, 8, 12, 14, 15
- [15] Stefan Hinterstoisser, Vincent Lepetit, Slobodan Ilic, Stefan Holzer, Gary Bradski, Kurt Konolige, and Nassir Navab. Model based training, detection and pose estimation of texture-less 3d objects in heavily cluttered scenes. In *Asian conference on computer vision*, pages 548–562. Springer, 2012. 1, 2, 5, 6, 7, 15
- [16] Tomáš Hodaň, Martin Sundermeyer, Bertram Drost, Yann Labbé, Eric Brachmann, Frank Michel, Carsten Rother, and Jiří Matas. Bop challenge 2020 on 6d object localization. In *European Conference on Computer Vision*, pages 577–594. Springer, 2020. 7
- [17] Berthold K. P. Horn, Hugh M. Hilden, and Shahriar Negahdaripour. Closed-form solution of absolute orientation using orthonormal matrices. *J. Opt. Soc. Am. A*, 5(7):1127–1135, Jul 1988. 5, 6
- [18] Yinlin Hu, Joachim Hugonot, Pascal Fua, and Mathieu Salzmann. Segmentation-driven 6d object pose estimation. In *Proceedings of the IEEE/CVF Conference on Computer Vision and Pattern Recognition*, pages 3385–3394, 2019. 1, 2, 3, 6, 7, 15
- [19] Wadim Kehl, Fabian Manhardt, Federico Tombari, Slobodan Ilic, and Nassir Navab. Ssd-6d: Making rgb-based 3d detection and 6d pose estimation great again. In *Proceedings of the IEEE international conference on computer vision*, pages 1521–1529, 2017. 1, 7, 14, 15
- [20] Yann Labbé, Justin Carpentier, Mathieu Aubry, and Josef Sivic. Cosypose: Consistent multi-view multi-object 6d pose estimation. In *European Conference on Computer Vision*, pages 574–591. Springer, 2020. 2
- [21] Y. Lamdan and H. J. Wolfson. Geometric hashing: A general and efficient model-based recognition scheme. In *[1988 Proceedings] Second International Conference on Computer Vision*, pages 238–249, 1988. 2

- [22] Yi Li, Gu Wang, Xiangyang Ji, Yu Xiang, and Dieter Fox. Deepim: Deep iterative matching for 6d pose estimation. In *Proceedings of the European Conference on Computer Vision (ECCV)*, pages 683–698, 2018. 7, 14
- [23] Tsung-Yi Lin, Michael Maire, Serge Belongie, James Hays, Pietro Perona, Deva Ramanan, Piotr Dollár, and C Lawrence Zitnick. Microsoft coco: Common objects in context. In *European conference on computer vision*, pages 740–755. Springer, 2014. 7
- [24] Jonathan Long, Evan Shelhamer, and Trevor Darrell. Fully convolutional networks for semantic segmentation. In *Proceedings of the IEEE conference on computer vision and pattern recognition*, pages 3431–3440, 2015. 3, 6
- [25] David G Lowe. Object recognition from local scale-invariant features. In *Proceedings of the seventh IEEE international conference on computer vision*, volume 2, pages 1150–1157. Ieee, 1999. 2
- [26] Fabian Manhardt, Diego Martin Arroyo, Christian Rupprecht, Benjamin Busam, Tolga Birdal, Nassir Navab, and Federico Tombari. Explaining the ambiguity of object detection and 6d pose from visual data. In *Proceedings of the IEEE/CVF International Conference on Computer Vision (ICCV)*, October 2019. 2
- [27] Fabian Manhardt, Wadim Kehl, Nassir Navab, and Federico Tombari. Deep model-based 6d pose refinement in rgb. In *Proceedings of the European Conference on Computer Vision (ECCV)*, pages 800–815, 2018. 7
- [28] M. Mohamad, M. T. Ahmed, D. Rappaport, and M. Greenspan. Super generalized 4pcs for 3d registration. In *2015 International Conference on 3D Vision*, pages 598–606, 2015. 2
- [29] M. Mohamad, D. Rappaport, and M. Greenspan. Generalized 4-points congruent sets for 3d registration. In *2014 2nd International Conference on 3D Vision*, volume 1, pages 83–90, 2014. 2
- [30] Markus Oberweger, Mahdi Rad, and Vincent Lepetit. Making deep heatmaps robust to partial occlusions for 3d object pose estimation. In *Proceedings of the European Conference on Computer Vision (ECCV)*, pages 119–134, 2018. 7, 15
- [31] Clark F. Olson. Efficient pose clustering using a randomized algorithm, 1997. 2
- [32] George Papandreou, Tyler Zhu, Liang-Chieh Chen, Spyros Gidaris, Jonathan Tompson, and Kevin Murphy. Personlab: Person pose estimation and instance segmentation with a bottom-up, part-based, geometric embedding model. In *Proceedings of the European Conference on Computer Vision (ECCV)*, pages 269–286, 2018. 8
- [33] Kiru Park, Timothy Patten, and Markus Vincze. Pix2pose: Pixel-wise coordinate regression of objects for 6d pose estimation. In *Proceedings of the IEEE/CVF International Conference on Computer Vision*, pages 7668–7677, 2019. 2, 7, 12, 14, 15
- [34] Kiru Park, Timothy Patten, and Markus Vincze. Neural object learning for 6d pose estimation using a few cluttered images. In Andrea Vedaldi, Horst Bischof, Thomas Brox, and Jan-Michael Frahm, editors, *Computer Vision – ECCV 2020*, pages 656–673, Cham, 2020. Springer International Publishing. 2, 12
- [35] Georgios Pavlakos, Xiaowei Zhou, Aaron Chan, Konstantinos G Derpanis, and Kostas Daniilidis. 6-dof object pose from semantic keypoints. In *2017 IEEE international conference on robotics and automation (ICRA)*, pages 2011–2018. IEEE, 2017. 1, 8
- [36] Sida Peng, Yuan Liu, Qixing Huang, Xiaowei Zhou, and Hujun Bao. Pvnnet: Pixel-wise voting network for 6dof pose estimation. In *Proceedings of the IEEE/CVF Conference on Computer Vision and Pattern Recognition*, pages 4561–4570, 2019. 1, 2, 3, 4, 6, 7, 8, 12, 14, 15
- [37] Charles R. Qi, Or Litany, Kaiming He, and Leonidas J. Guibas. Deep hough voting for 3d object detection in point clouds. In *Proceedings of the IEEE/CVF International Conference on Computer Vision (ICCV)*, October 2019. 1, 2, 3, 4, 8
- [38] Charles R Qi, Li Yi, Hao Su, and Leonidas J Guibas. Pointnet++: Deep hierarchical feature learning on point sets in a metric space. *arXiv preprint arXiv:1706.02413*, 2017. 4
- [39] Long Quan and Zhongdan Lan. Linear n-point camera pose determination. *IEEE Transactions on pattern analysis and machine intelligence*, 21(8):774–780, 1999. 8
- [40] Mahdi Rad and Vincent Lepetit. Bb8: A scalable, accurate, robust to partial occlusion method for predicting the 3d poses of challenging objects without using depth. In *Proceedings of the IEEE International Conference on Computer Vision*, pages 3828–3836, 2017. 8
- [41] Joseph Redmon and Ali Farhadi. Yolov3: An incremental improvement. *arXiv preprint arXiv:1804.02767*, 2018. 2
- [42] Fred Rothganger, Svetlana Lazebnik, Cordelia Schmid, and Jean Ponce. 3d object modeling and recognition using local affine-invariant image descriptors and multi-view spatial constraints. *International journal of computer vision*, 66(3):231–259, 2006. 1
- [43] Jianzhun Shao, Yuhang Jiang, Gu Wang, Zhigang Li, and Xiangyang Ji. Pfrl: Pose-free reinforcement learning for 6d pose estimation. In *IEEE/CVF Conference on Computer Vision and Pattern Recognition (CVPR)*, June 2020. 2
- [44] Bugra Tekin, Sudipta N Sinha, and Pascal Fua. Real-time seamless single shot 6d object pose prediction. In *Proceedings of the IEEE Conference on Computer Vision and Pattern Recognition*, pages 292–301, 2018. 1, 7, 8, 14, 15
- [45] Ameni Trabelsi, Mohamed Chaabane, Nathaniel Blanchard, and Ross Beveridge. A pose proposal and refinement network for better 6d object pose estimation. In *Proceedings of the IEEE/CVF Winter Conference on Applications of Computer Vision*, pages 2382–2391, 2021. 2, 7, 12, 14, 15
- [46] Jonathan Tremblay, Thang To, Balakumar Sundaralingam, Yu Xiang, Dieter Fox, and Stan Birchfield. Deep object pose estimation for semantic robotic grasping of household objects. *arXiv preprint arXiv:1809.10790*, 2018. 1
- [47] Chen Wang, Danfei Xu, Yuke Zhu, Roberto Martín-Martín, Cewu Lu, Li Fei-Fei, and Silvio Savarese. Densefusion: 6d object pose estimation by iterative dense fusion. In *Proceedings of the IEEE/CVF Conference on Computer Vision and Pattern Recognition*, pages 3343–3352, 2019. 7, 8, 12, 14, 15

- [48] Gu Wang, Fabian Manhardt, Jianzhun Shao, Xiangyang Ji, Nassir Navab, and Federico Tombari. Self6d: Self-supervised monocular 6d object pose estimation. In *European Conference on Computer Vision*, pages 108–125. Springer, 2020. 2, 12
- [49] Yu Xiang, Tanner Schmidt, Venkatraman Narayanan, and Dieter Fox. Posecnn: A convolutional neural network for 6d object pose estimation in cluttered scenes. 2018. 1, 2, 3, 6, 7, 8, 12, 15
- [50] Sergey Zakharov, Ivan Shugurov, and Slobodan Ilic. Dpod: 6d pose object detector and refiner. In *Proceedings of the IEEE/CVF International Conference on Computer Vision*, pages 1941–1950, 2019. 2, 7, 12, 14, 15

## Appendix A. Overview

We document here some addition implementation details, results and further ablation studies. In Sec. B, complete details of the Fully Convolutional ResNet backbone are provided, in sufficient detail to recreate the network. In Sec. C, the 6 DoF pose estimation accuracy results for each object is presented, as well as some extra bounding box image samples. Finally in Sec. D, three additional ablation studies are included investigating the impact of the number of skip connections in the backbone network, the depth of the network, as well as the impact of combining the three different voting schemes into various multi-scheme voting configurations.

## Appendix B. ResNet Backbone Structure

As shown in Table 8, we modified ResNet to a Fully Convolutional Network. To start with, we replaced the Fully Connected Layer with a convolutional layer for the following up sampling layers. We then applied up-sampling to the feature map with a combination of convolution, bilinear interpolations, and skip concatenations from the residual blocks. We apply more skip layers than did PVNet [36], under the assumption that the convolutional feature maps would preserve more local features than the alternative bilinear interpolation, especially for deeper small scale feature maps. This design was supported by the ablation study described in Sec. D.1.

## Appendix C. Accuracy Results Per Object

The detailed LINEMOD, Occlusion LINEMOD ADD(s) results, and the YCB-Video ADD(s) and AUC results categorized per object are listed in Table 9, Table 10 and Table 11, respectively. Some additional successful images showing recovered and ground truth bounding boxes are displayed in Figure 8.

As can be seen in Table 9, the original LINEMOD dataset is mostly saturated, with results from a number of different methods that are close to perfect. Nevertheless, RCVPose+ICP outperformed all alternatives at 99.7%, with 100% ADD(s) for three objects, including the only perfect scores for driller and holepuncher.

The results in Table 10 show Occlusion LINEMOD is to be quite challenging. This is not only just because of the occluded scenes, but is also due to the fact that the meshes are not very precisely modelled, and some ground truth poses are not accurate for some cases.

The YCB-Video dataset has two evaluation metrics, as shown in Table 11. In general, AUC is more forgiving than ADD(s) since AUC has a tolerance of up to 10 cm [49]. For some objects like the master chef can and the power drill, RCVPose performs slightly worse in AUC compared to PVN3D[14], while still performing better in ADD(s).

	# of skip connections			
	3		5	
	$\mu$	$\sigma$	$\mu$	$\sigma$
ape	2.4	1.1	1.8	0.8
driller	3.6	1.2	2.7	0.8
eggbox	3.5	1.7	2.4	1.2

Table 7. Average keypoint estimation error mean ( $\mu$  [mm]) and standard deviation ( $\sigma$  [mm]) for different ResNet-18 backbone skip connections. Increasing the skip connections reduced the error of the estimation.

## Appendix D. Extra Ablation Studies

### D.1. Number of Skip Connections

There were five different network architectures proposed in the initial ResNet paper [13]. While some 6 DoF pose recovery works use variations of ResNet-18 [36, 47, 50, 45] others use ResNet-50 [48, 34]. Some customize the structure by converting it to encoder [45, 34, 50, 47], adding extra layers and skip connections [36] while others use the original ResNet unaltered [14, 33].

We conducted an experiment which examined the impact of the number of skip connections on mean keypoint estimation error  $\bar{e}$ . We increased the number of skip connections for ResNet-18, from 3 to 5. Skip connections improve the influence of image features during upsampling. The results are displayed in Table D.1, and show that increasing the skip connections from 3 to 5, decreased both the mean and the standard deviation of the keypoint estimation error decreased by a large margin, in all cases.

### D.2. ResNet Backbone Depth

A further experiment tested different ResNet depths, from 18 to 152 layers. The results are plotted in Fig. 7, and indicate that the substantially deeper networks exhibit only a minor reduction in  $\bar{e}$ .

Despite the rather minor improvement due to increased depth, we nevertheless used ResNet-152 with 5 skip connections in the RCVPose in our experiments. It is likely that we would have received very similar results had we based our backbone network on ResNet-18, albeit with a faster training cycle and smaller memory footprint.

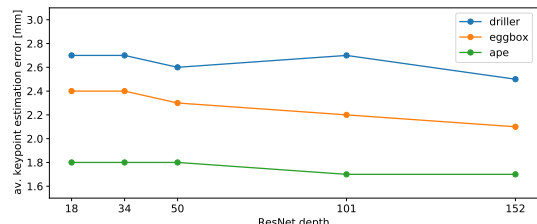


Figure 7. Mean keypoint estimation error [mm] vs. ResNet depth.



### D.3. Multi-scheme Voting

The accumulator space is represented exactly the same for all three voting schemes, and is handled in exactly the same manner to extract keypoint locations through peak detection, once the voting has been completed. It is therefore possible and straightforward to combine voting schemes, by simply adding their resulting accumulator spaces prior to peak detection.

We implemented this and compared the impact of all possible combinations of offset, vector, and radial voting schemes. The results are shown in Table 12, which also includes the results from each individual voting scheme for comparison. It can be seen that the radial voting scheme outperforms all other alternatives, yielding a lower mean and standard deviation of keypoint estimation error  $\bar{\epsilon}$ .

ResNet Backbone Structure															
Layer	ResNet-152 32s(RCVPose)			ResNet-101 32s			ResNet-50 32s			ResNet-34 32s		ResNet-18 32s		ResNet-18 8s(PVNet)	
conv1	$7 \times 7, 64, \text{stride } 2$														
conv2	$3 \times 3 \text{ max pool, stride } 2$														
		$\begin{bmatrix} 1 \times 1, 64 \\ 3 \times 3, 64 \\ 1 \times 1, 256 \end{bmatrix} \times 3$		$\begin{bmatrix} 1 \times 1, 64 \\ 3 \times 3, 64 \\ 1 \times 1, 256 \end{bmatrix} \times 3$		$\begin{bmatrix} 1 \times 1, 64 \\ 3 \times 3, 64 \\ 1 \times 1, 256 \end{bmatrix} \times 3$		$\begin{bmatrix} 3 \times 3, 64 \\ 3 \times 3, 64 \end{bmatrix} \times 3$		$\begin{bmatrix} 3 \times 3, 64 \\ 3 \times 3, 64 \end{bmatrix} \times 2$		$\begin{bmatrix} 3 \times 3, 64 \\ 3 \times 3, 64 \end{bmatrix} \times 2$			
conv3		$\begin{bmatrix} 1 \times 1, 128 \\ 3 \times 3, 128 \\ 1 \times 1, 512 \end{bmatrix} \times 8$		$\begin{bmatrix} 1 \times 1, 128 \\ 3 \times 3, 128 \\ 1 \times 1, 512 \end{bmatrix} \times 4$		$\begin{bmatrix} 1 \times 1, 128 \\ 3 \times 3, 128 \\ 1 \times 1, 512 \end{bmatrix} \times 4$		$\begin{bmatrix} 3 \times 3, 128 \\ 3 \times 3, 128 \end{bmatrix} \times 4$		$\begin{bmatrix} 3 \times 3, 128 \\ 3 \times 3, 128 \end{bmatrix} \times 2$		$\begin{bmatrix} 3 \times 3, 128 \\ 3 \times 3, 128 \end{bmatrix} \times 2$			
conv4		$\begin{bmatrix} 1 \times 1, 256 \\ 3 \times 3, 256 \\ 1 \times 1, 1024 \end{bmatrix} \times 36$		$\begin{bmatrix} 1 \times 1, 256 \\ 3 \times 3, 256 \\ 1 \times 1, 1024 \end{bmatrix} \times 23$		$\begin{bmatrix} 1 \times 1, 256 \\ 3 \times 3, 256 \\ 1 \times 1, 1024 \end{bmatrix} \times 6$		$\begin{bmatrix} 3 \times 3, 256 \\ 3 \times 3, 256 \end{bmatrix} \times 6$		$\begin{bmatrix} 3 \times 3, 256 \\ 3 \times 3, 256 \end{bmatrix} \times 2$		$\begin{bmatrix} 3 \times 3, 256 \\ 3 \times 3, 256 \end{bmatrix} \times 2$			
conv5		$\begin{bmatrix} 1 \times 1, 512 \\ 3 \times 3, 512 \\ 1 \times 1, 2048 \end{bmatrix} \times 3$		$\begin{bmatrix} 1 \times 1, 512 \\ 3 \times 3, 512 \\ 1 \times 1, 2048 \end{bmatrix} \times 3$		$\begin{bmatrix} 1 \times 1, 512 \\ 3 \times 3, 512 \\ 1 \times 1, 2048 \end{bmatrix} \times 3$		$\begin{bmatrix} 3 \times 3, 512 \\ 3 \times 3, 512 \end{bmatrix} \times 3$		$\begin{bmatrix} 3 \times 3, 512 \\ 3 \times 3, 512 \end{bmatrix} \times 2$		$\begin{bmatrix} 3 \times 3, 512 \\ 3 \times 3, 512 \end{bmatrix} \times 2$			
conv6	$3 \times 3, \text{stride } 1, \text{padding } 1$ batch norm ReLU														
up5				$\text{conv } 3 \times 3, \text{stride } 1, \text{padding } 1$ batch norm ReLU bilinear interpolation											
up4				$\text{conv } 3 \times 3, \text{stride } 1, \text{padding } 1$ batch norm ReLU bilinear interpolation											
up3				$\text{conv } 3 \times 3, \text{stride } 1, \text{padding } 1$ batch norm ReLU bilinear interpolation						$\text{conv } 3 \times 3, \text{stride } 1, \text{padding } 1$ batch norm Leaky ReLU bilinear interpolation					
up2				$\text{conv } 3 \times 3, \text{stride } 1, \text{padding } 1$ batch norm ReLU bilinear interpolation						$\text{conv } 3 \times 3, \text{stride } 1, \text{padding } 1$ batch norm Leaky ReLU bilinear interpolation					
up1				$\text{conv } 3 \times 3, \text{stride } 1, \text{padding } 1$ batch norm ReLU bilinear interpolation						$\begin{bmatrix} \text{conv } 3 \times 3, \text{stride } 1, \text{padding } 1 \\ \text{batch norm} \\ \text{Leaky ReLU} \\ \text{bilinear interpolation} \end{bmatrix}$					
conv7				$3 \times 3, \text{stride } 1, \text{padding } 1$ batch norm ReLU						$3 \times 3, \text{stride } 1, \text{padding } 1$ batch norm Leaky ReLU					
conv8	$1 \times 1, \text{stride } 1, \text{padding } 0$											$1 \times 1, \text{stride } 1, \text{padding } 0$			

Table 8. ResNet Backbone structure compared to PVNet

Mode	Method	Object													
		ape	bench-vise	camera	can	cat	driller	duck	eggbox*	glue*	hole-puncher	iron	lamp	phone	mean
RGB	SSD6D+ref [19]	2.6	15.1	6.1	27.3	9.3	12.0	1.3	2.8	3.4	3.1	14.6	11.4	9.7	9.1
	Pix2Pose [33]	58.1	91	60.9	84.4	65	76.3	43.8	96.8	79.4	74.8	83.4	82	45	72.4
	DPOD [50]	53.3	95.3	90.4	94.1	60.4	97.7	66	99.7	93.8	65.8	99.8	88.1	74.2	83.0
	PVNet [36]	43.62	99.9	86.9	95.5	79.3	96.4	52.6	99.2	95.7	81.9	98.9	99.3	92.4	86.3
	PPRN [45]	84.5	98.7	93.7	97.8	87.3	96.9	88.5	98.5	99.5	84.5	99.1	98.7	92.5	93.9
	DeepIM [22]	77	97.5	93.5	96.5	82.1	95.0	77.7	97.1	99.4	52.8	98.3	97.5	87.7	88.6
RGB +D ref	YOLO6D [44]	21.6	81.8	36.6	68.8	41.8	63.5	27.2	69.6	80	42.6	75	71.1	47.7	56.0
	SSD6D+ref [19]	-	-	-	-	-	-	-	-	-	-	-	-	-	34.1
	DPOD+ref [50]	87.7	98.5	96.1	99.7	94.7	98.8	86.3	99.9	96.8	86.8	100	96.8	94.7	95.2
RGB-D	DenseFusion [47]	92.3	93.2	94.4	93.1	96.5	87.0	92.3	99.8	100.0	92.1	97.0	95.3	92.8	94.3
	PVN3D [14]	97.3	99.7	99.6	<b>99.5</b>	<b>99.8</b>	99.3	98.2	99.8	100.0	99.9	99.7	<b>99.8</b>	99.5	99.4
	RCVPose	99.2	99.6	99.7	99	99.4	99.7	99.4	98.7	99.7	99.8	99.9	99.2	99.1	99.43
	RCVPose+ICP	<b>99.6</b>	<b>99.7</b>	<b>99.7</b>	99.3	99.7	<b>100</b>	<b>99.7</b>	99.3	<b>100.0</b>	<b>100</b>	<b>99.9</b>	99.5	<b>99.7</b>	<b>99.7</b>

Table 9. LINEMOD Accuracy Results: Non-symmetric objects are evaluated with ADD, and symmetric objects (annotated with \*) are evaluated with ADD-s.

Mode	Method	Object								ADD(s)[%]
		ape	can	cat	driller	duck	eggbox*	glue*	holepuncher	
RGB	Oberweger [30]	12.1	39.9	8.2	45.2	17.2	22.1	35.8	36.0	27.1
	Hu et al. [18]	17.6	53.9	3.3	62.4	19.2	25.9	39.6	21.3	30.4
	Pix2Pose [33]	22.0	44.7	22.7	44.7	15.0	25.2	32.4	49.5	32.0
	DPOD [50]	-	-	-	-	-	-	-	-	32.8
	PVNet [36]	15.8	63.3	16.7	25.2	<b>65.7</b>	50.2	49.6	39.7	40.8
	PPRN [45]	-	-	-	-	-	-	-	-	58.4
RGB +D ref	YOLO6D [44]	-	-	-	-	-	-	-	-	6.4
	SSD6D+ref [19]	-	-	-	-	-	-	-	-	27.5
	PoseCNN [49]	9.6	45.2	0.9	41.4	19.6	22.0	38.5	22.1	24.9
	DPOD+ref [50]	-	-	-	-	-	-	-	-	47.3
RGB-D	PVN3D [14]	33.9	88.6	39.1	78.4	41.9	80.9	68.1	74.7	63.2
	RCVPose	60.3	92.5	50.2	78.2	52.1	81.2	72.1	75.2	70.2
	RCVPose+ICP	<b>61.3</b>	<b>93</b>	<b>51.2</b>	<b>78.8</b>	53.4	<b>82.3</b>	<b>72.9</b>	<b>75.8</b>	<b>71.1</b>

Table 10. Occlusion LINEMOD Accuracy Results. Non-symmetric objects are evaluated with ADD, and symmetric objects (annotated with \*) are evaluated with ADD-s.

Refine	Metric	Method	002 master cylinder can	003 crescent box	004 sugar box	005 tomato soup can	006 mustard bottle	007 tuna fish can	008 piddling fox	009 glass box	010 potted plant can	011 banana	019 pitcher bottle	021 bleach cylinder	024 bowl*	025 mug	035 power drill	036 wood block*	037 scissors	040 large hammer	051 large clamp*	052 extra large clamp*	061 foghorn rocket*	mean
No	AUC	PoseCNN [49]	83.9	76.9	84.2	81.0	90.4	88.0	79.1	87.2	78.5	86.0	77.0	71.6	69.6	78.2	72.7	64.3	56.9	71.7	50.2	44.1	88.0	75.8
		DF(per-pixel)[47]	95.3	92.5	95.1	93.8	95.8	95.7	94.3	97.2	89.3	90.0	93.6	94.4	86.0	95.3	92.1	89.5	90.1	95.1	71.5	70.2	92.2	91.2
		PVN3D[14]	<b>96.0</b>	96.1	97.4	96.2	97.5	96	97.1	97.7	93.3	96.6	<b>97.4</b>	96.0	90.2	97.6	<b>96.7</b>	<b>90.4</b>	<b>96.7</b>	<b>96.7</b>	93.6	88.4	<b>96.8</b>	95.5
		RCVPose	95.7	<b>97.2</b>	<b>97.6</b>	<b>98.2</b>	<b>97.9</b>	<b>98.2</b>	<b>97.7</b>	<b>97.7</b>	<b>97.9</b>	<b>97.9</b>	96.2	<b>99.2</b>	<b>95.2</b>	<b>98.4</b>	96.2	89.1	96.2	95.9	<b>95.2</b>	<b>94.7</b>	95.7	<b>96.6</b>
	ADD (s)	PoseCNN [49]	50.2	53.1	68.4	66.2	81.0	70.7	62.7	75.2	59.5	72.3	53.3	50.3	69.6	58.5	55.3	64.3	35.8	58.3	50.2	44.1	88.0	59.9
		DF(per-pixel)[47]	70.7	86.9	90.8	84.7	90.9	79.6	89.3	95.8	79.6	76.7	87.1	87.5	86.0	83.8	83.7	89.5	77.4	89.1	71.5	70.2	92.2	82.9
Yes	AUC	PVN3D[14]	80.5	94.8	96.3	88.5	96.2	89.3	95.7	96.1	88.6	93.7	<b>96.5</b>	93.2	90.2	95.4	95.1	<b>90.4</b>	92.7	91.8	93.6	88.4	<b>96.8</b>	91.8
		RCVPose	<b>93.6</b>	<b>95.7</b>	<b>97.2</b>	<b>94.7</b>	<b>97.2</b>	<b>96.4</b>	<b>97.1</b>	<b>96.5</b>	<b>90.2</b>	<b>96.7</b>	95.7	<b>97.8</b>	<b>94.9</b>	<b>96.3</b>	<b>95.4</b>	89.3	<b>94.7</b>	<b>92.4</b>	<b>96.4</b>	<b>94.7</b>	95.7	<b>95.2</b>
		PoseCNN [49]+ICP	95.8	92.7	98.2	94.5	98.6	97.1	97.9	98.8	92.7	97.1	97.8	96.9	81.0	94.9	98.2	87.6	91.7	97.2	75.2	64.4	97.2	93.0
		DF(Iterative)[47]	96.4	95.8	97.6	94.5	97.3	97.1	96.0	98.0	90.7	96.2	97.5	95.9	89.5	96.7	96.0	92.8	92.0	97.6	72.5	69.9	92.0	93.2
	ADD (s)	PVN3D[14]+ICP	95.2	94.4	97.9	95.9	<b>98.3</b>	96.7	<b>98.2</b>	<b>98.8</b>	93.8	98.2	<b>97.6</b>	97.2	92.8	97.7	<b>97.1</b>	<b>91.1</b>	95.0	98.1	95.6	90.5	<b>98.2</b>	96.1
		RCVPose+ICP	<b>96.2</b>	<b>97.9</b>	97.9	<b>99</b>	98.2	<b>98.6</b>	98.1	98.4	<b>98.4</b>	<b>98.3</b>	97.2	<b>99.6</b>	<b>96.9</b>	<b>98.7</b>	96.4	90.7	<b>96.4</b>	<b>96.6</b>	<b>96.2</b>	<b>95.1</b>	96.6	<b>97.2</b>
		PoseCNN [49]+ICP	68.1	83.4	97.1	81.8	98.0	83.9	96.6	98.1	83.5	91.9	96.9	92.5	81.0	81.1	97.7	87.6	78.4	85.3	75.2	64.4	97.2	85.4
		DF(Iterative)[47]	73.2	94.1	96.5	85.5	94.7	81.9	93.3	96.7	83.6	83.3	96.9	89.9	89.5	88.9	92.7	92.8	77.9	93.0	72.5	69.9	92.0	86.1
Yes	ADD (s)	PVN3D[14]+ICP	79.3	91.5	96.9	89.0	<b>97.9</b>	90.7	97.1	<b>98.3</b>	87.9	96.0	<b>96.9</b>	95.9	92.8	96.0	95.7	91.1	87.2	91.6	95.6	90.5	<b>98.2</b>	92.3
		RCVPose+ICP	<b>94.7</b>	<b>96.4</b>	<b>97.6</b>	<b>95.4</b>	97.7	<b>96.7</b>	<b>97.4</b>	97.9	<b>92.6</b>	<b>97.2</b>	96.7	<b>98.4</b>	<b>95.3</b>	<b>97.1</b>	<b>96.2</b>	<b>91.2</b>	<b>94.9</b>	<b>93.2</b>	<b>96.7</b>	<b>94.9</b>	96.6	<b>95.9</b>

Table 11. YCB Video AUC [49] and ADD(s) [15] results: Non-symmetric objects are evaluated with ADD, and symmetric objects (annotated with \*) are evaluated with ADD-s. The AUC metrics is based on the curve with ADD for non-symmetries and ADDs with symmetries.

		$\bar{\epsilon}$ [mm]													
	$\bar{r}$ [mm]	vector+offset		vector+radial		radial+offset		vector+offset+radial		vector		offset		radial	
		$\mu_v$	$\sigma_v$	$\mu_o$	$\sigma_o$	$\mu_r$	$\sigma_r$	$\mu_r$	$\sigma_r$	$\mu_r$	$\sigma_r$	$\mu_r$	$\sigma_r$	$\mu_r$	$\sigma_r$
ape	142.1	20.2	12.4	12.7	6.7	9.8	6.2	7.2	1.2	12.5	7.6	10.4	5.3	1.8	0.8
driller	318.8	22.3	11.7	13.3	7.9	8.7	3.4	5.7	2.3	11.3	8.2	9.5	3.5	2.7	0.8
eggbox	197.3	21.6	13.5	17.4	10.5	12.1	5.2	6.4	3.3	13.7	8.5	11.4	4.7	2.4	1.2

Table 12. Combined Accumulator Space:  $\bar{\epsilon}$  mean ( $\mu_{\{v|o|r\}}$ ) and standard deviation ( $\sigma_{\{v|o|r\}}$ ) for different combination of 3 voting schemes, with  $\bar{r}$  = mean distance of keypoints to object centroid.



Figure 8. Occluded LINEMOD sample results: Blue box = ground truth, green box = estimate.